ARTICLE

Ultrasensitive optofluidic enzyme-linked immunosorbent assay by on-chip integrated polymer whispering-gallery-mode microlaser sensors

Received 00th January 20xx,
Accepted 00th January 20xx

DOI: 10.1039/x0xx00000x

Xia Ouyang,[a] Tong Liu,[a] Yangxi Zhang,[a] Jijun He,[ab] Zijian He,[a] A. Ping Zhang*[a] and Hwa-Yaw Tam[a]

Optical whispering-gallery-mode (WGM) microcavities offer great promise in ultrasensitive biosensors because of their unique ability to enable resonant recirculation of light to achieve strong light-matter interactions in microscale volumes. However, it remains a challenge to develop cost-effective, high-performance WGM microcavity-based biosensing devices for practical disease diagnosis applications. In this paper, we present an optofluidic chip that is integrated with directly-printed, high-quality-factor (Q) polymer WGM microlaser sensors for ultrasensitive enzyme-linked immunosorbent assay (ELISA). Optical 3D μ-printing technology based on maskless ultraviolet lithography is developed to rapidly fabricate high-Q suspended-disk WGM microcavities. After deposition with a thin layer of optical gain material, low-threshold WGM microlasers are fabricated and then integrated together with optical fibres upon a microfluidic chip to achieve an optofluidic device. With flexible microfluidic technology, on-chip, integrated, WGM microlasers are further modified *in situ* with biomolecules on surface for highly selective biomarker detection. It is demonstrated that such an optofluidic biochip can measure horseradish peroxidase (HRP)-streptavidin, which is a widely used catalytic molecule in ELISA, via chromogenic reaction at the concentration level of 0.3 ng/mL. Moreover, it enables on-chip optofluidic ELISA of the disease biomarker vascular endothelial growth factor (VEGF) at the extremely low concentration level of 17.8 fg/mL, which is over 2 orders of magnitude better than the ability of current commercial ELISA kits.

Introduction

Quantitative detection of biomarkers has become increasingly important for the diagnosis of diseases, particularly for early-stage disease detection.[1] Because of its distinct merits of high sensitivity and high specificity, enzyme-linked immunosorbent assay (ELISA) has been deemed the gold standard for biomarker analysis.[2] Derived from the enzyme immunoassay method, ELISA quantifies the target analyte by a signal associated with an antibody-linked enzyme whose ligand can specifically bind to the detection reagent.[3] Due to the high reliability of ligand binding interactions, a target analyte in a liquid sample can be selectively detected at a very low level.[4] However, the detection limit of current commercial ELISA products is on the level of several pg/mL,[5] which cannot meet the requirement of many early-stage disease diagnosis applications. For example, to determine age-related macular degeneration, one needs to detect and analyse vascular endothelial growth factor (VEGF), which is a hypoxia-inducible protein whose abnormal expression is associated with many diseases, in the aqueous humour of the eyeball at levels as low as 10^{-14} g/mL.[6] Therefore, demand has been increasing for the improvement of the ability of ELISA regarding a lower detection limit.

One of the promising solutions to improve ELISA is micro/nano-photonic technologies.[7-9] In particular, high-quality whispering-gallery-mode (WGM) microcavities with very low loss are one of the leading candidates because of their unique ability to build up very strong in-cavity light for investigation of light-matter interactions,[10] and thus have great potential in biochemical sensing and lab-on-a-chip applications, such as on-chip polymerase chain reaction.[11] One of the inherent abilities of optical WGM microcavity techniques is their ability to achieve low-threshold laser oscillation,[12] because of the low intracavity loss and small mode volume.[13, 14] Compared with passive optical microcavities, which mainly rely on fragile evanescent-wave coupling techniques,[15] WGM microcavity lasers also exhibit an advantageous coupling strategy, i.e., free-space coupling.[16, 17] They can alleviate coupling difficulties and thus offer more flexibility to overcome the obstacles of on-chip integration to achieve photonic-integrated biosensing platforms.[18] Because of the advantages of a narrow linewidth and high-contrast ratio of output spectral peaks, WGM microlasers have been demonstrated to develop ultrasensitive biosensors for the detection of proteins, lipids, DNA, and viruses.[19-23] However, the fabrication of high-quality WGM microcavity lasers usually requires advanced microfabrication technologies to create 3D structures at the micrometer scale. Various technologies, such as mask-based photolithography,[24] E-beam lithography,[25] and direct femtosecond laser writing,[26] have been utilized in the

[a] *Photonics Research Centre, Department of Electrical Engineering, The Hong Kong Polytechnic University, Hong Kong SAR, China. E-mail: azhang@polyu.edu.hk*
[b] *Institute of Physics, École Polytechnique Fédérale de Lausanne (EPFL), CH-1015 Lausanne, Switzerland.*
†Electronic Supplementary Information (ESI) available: See DOI: 10.1039/x0xx00000x

fabrication of WGM biosensors. All of these technologies are costly or time-consuming[27] and thus hinder the applications of WGM microlasers in the development of cost-effective, high-performance biosensors for the practical diagnosis of early-stage diseases.

In this paper, we present an approach for rapidly printing high-quality polymer WGM microlaser sensors that were then integrated into a microfluidic chip to achieve the first, to the best of our knowledge, polymer WGM microlaser-based optofluidic biochip for ELISA, as shown in Fig. 1, for the ultrasensitive detection of biomarkers. With an in-house, digital mirror device (DMD)-based optical 3D μ-printing technology,[28] we develop an improved process technology to rapidly print polymer WGM microcavities of suspended microdisks with finer profiles and a relatively high quality factor (*Q*-factor). After deposition of a thin layer of optical gain materials, very low-threshold WGM microlasers, whose laser oscillation can operate at the pump pulse energy of 25.06 nJ/mm^2, were fabricated. WGM microlasers were then integrated together with multimode optical fibres (MMOFs) upon a microfluidic chip to achieve an optofluidic platform for on-chip ELISA. Experimental results showed that such a compact and cost-effective polymer WGM microlaser-based optofluidic ELISA biochip can detect VEGF at the extremely low detection limit of 17.8 fg/mL, which is over 2 orders of magnitude lower than that of commercial ELISA products and comparable to the result based on expensive surface-enhanced Raman spectroscopy.[29]

Methods and materials

Materials

EPON resins SU-8 and SU8-2100 were purchased from Momentive Performance Materials and MicroChem, respectively. OPPI SbF_6 (OPPI) was purchased from Hampford Research. TINUVIN 234 was purchased from Sigma-Aldrich. Tributylamine (TBA) was purchased from Meryer Chemical Technology. Rhodamine 6G (Rh6G) was purchased from Exciton. Ethanol, cyclopentanone, propylene glycol methyl ether acetate (PGMEA) and (3-aminopropyl)triethoxysilane (APTES) were purchased from J&K Scientific. Polydimethylsiloxane (PDMS) and its curing agent were obtained from Dow Corning. 3,3',5,5'-Tetramethylbenzidine (TMB) colour reagents A and B and horseradish peroxidase-conjugated streptavidin (HRP-streptavidin) were purchased from Solarbio Science & Technology. For ELISA, biotinylated detection antibody and HRP-streptavidin were obtained from R&D Systems (ELISA Kit catalogue number: DY293B-05). Tween 20 was purchased from Biofroxx. Phosphate buffered solution (PBS) and bovine serum albumin (BSA) were ordered from Sigma-Aldrich. DI water with a resistance of 18 MΩ·cm was used in all experiments.

Fabrication and characterization of polymer WGM microcavities

The polymer WGM microcavities were fabricated by an in-house optical 3D μ-printing platform (Fig. S1a), which consisted of a high-power UV light source (OmniCure 2000 System, Lumen Dynamic Group Inc.), a DMD (DLi4120 0.7" XGA, Texas Instruments, USA), projection optics, and a high-precision motorized X-Y stage (M-687, Physik Instrumente GmbH & Co.).

EPON resin SU-8 was used in the fabrication of WGM microcavities. SU-8, photo-initiator (OPPI), inhibitor (TBA), and

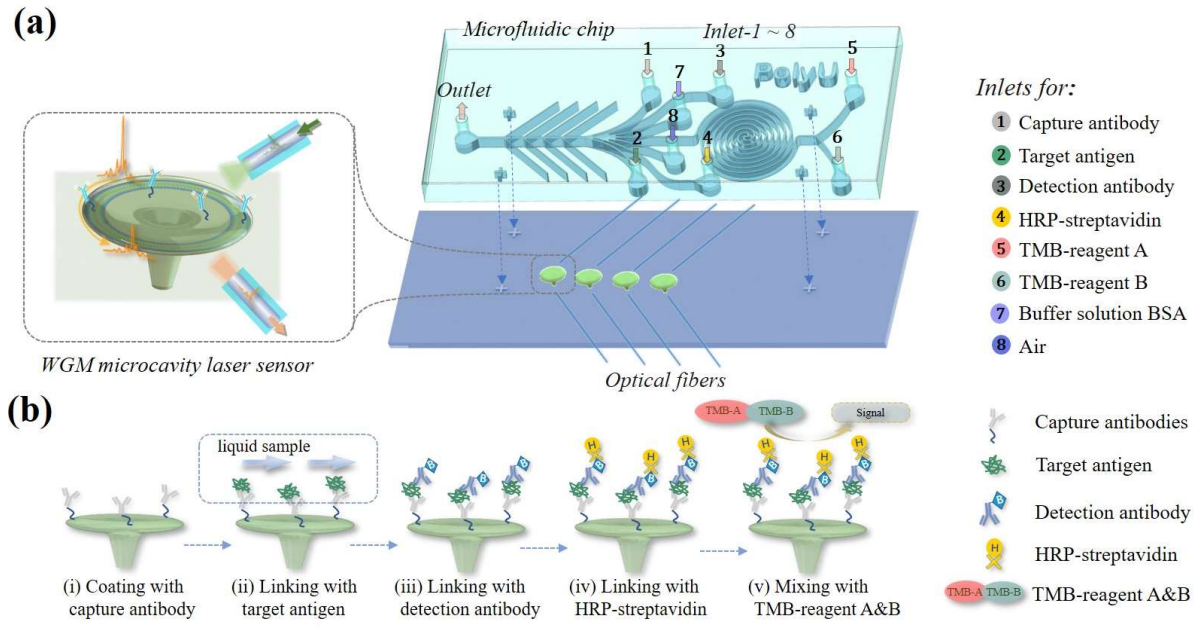

Fig. 1 Schematic of the WGM microlaser-integrated optofluidic chip for ELISA. The microfluidic chip contains: eight inlets for injection of different reagents; microchannels for delivering reagents and integration of WGM microlaser sensors; one spiral mixer for mixing reagents; fishbone-shaped grooves for embedding of optical fibers; one outlet for collection of liquids after reaction. (b) Workflow of in situ modifications of the surface of a WGM microlaser with functional molecules for on-chip optofluidic ELISA of VEGF.

UV absorber (TINUVIN 234) were mixed at the weight ratio of SU-8/OPPI/TBA/TINUVIN 234 = 100:2.5:0.014:0.08. Image data sliced from the 3D model of the WGM microcavities were used to drive DMD for crate dynamic optical patterns for exposure of the prepared SU-8 resin after scaling down via projection optics. After the exposure, the photo-activated SU-8 resin was cured by post-baking and developed by PGMEA for 10 min. Optical exposure processes were optimized through the establishment of a precise relation between exposure dose and cured depth, as shown in Fig. S1b. The cured depth was measured to be linearly proportional to the logarithm of exposure time, which is consistent with the Beer-Lambert law.

The fabricated WGM microcavities were optically characterized by measuring the transmission spectra. A tapered optical fibre with a waist diameter of approximately 1.3 μm was fabricated by using a fibre tapering system (Vytran GPX-3400, Thorlabs Inc.) and then used to couple light with the optical microcavities. The alignment was conducted using a piezo-motorized stage (MAX312D, Thorlabs Inc.). A broadband light source (1420~1620 nm) and an optical spectrum analyser with a resolution of 0.02 nm (AQ6370D, Yokogawa Co.) were used in the measurement of transmission spectra.

Fabrication and testing of WGM microlasers

Laser dye Rh6G was used to coat the surface of the WGM microcavity to fabricate WGMLs. Rh6G was first dissolved in ethanol at a concentration of 20 μmol/mL and then mixed with SU-8 resin in cyclopentanone to prepare an SU-8 solution in which the concentration of Rh6G was 3 μmol/g. A thin layer of Rh6G-doped SU-8 was spin-coated on the WGM microcavities and then soft-baked at 65 °C for 15 min to remove any solvent. Fluorescence images of active WGM microcavities were acquired via fluorescence microscopy (Eclipse 80i, Nikon Instruments Inc.) with excitation by a continuous-wave laser at a central wavelength of 532 nm.

Optical pumping tests of the active WGM microcavities were conducted by using a frequency-doubled Nd:YAG pulsed laser (Inlite II, Continuum Ltd.) at the centre wavelength of 532 nm. The pulse duration and repetition rate of the laser were 10 ns and 10 Hz, respectively. The pump laser beam converged into a MMOF with a core diameter of 105 μm (BGWU-105, Shouliang Ltd.) via an objective, and another MMOF with the same parameters was used to collect light from the equatorial plane of the WGM microcavity. The emission spectra of the WGMLs were acquired by using an MMOF-connected spectrometer (SpectraPro 2750, Princeton Instruments Ltd.).

Fabrication of the microfluidic chip

The microfluidic chip was designed with eight inlets, one spiral mixer and one outlet for injection, mixing and collection of reagents, respectively. Here, the spiral mixer is a rotation-based passive mixer that can generate transverse flows across the cross-section of microchannel so as to fully mix reagents. The microfluidic chip was fabricated by using PDMS with the casting method. The mould of the microchannels was prepared by using SU-8, as shown in Fig. S2. The size of the mould was 40 mm × 18 mm, and its height was approximately 150 μm, which was chosen for ease of integration with MMOFs. The PDMS precursor was mixed with the curing agent at a ratio of 11:1, which was slightly higher than the common ratio to achieve PDMS with a lower Young's modulus. The mixture was then poured upon the prepared SU-8 mould and cured in an oven at 70 °C for 2 h after degassing. The cured PDMS with microfluidic channels was peeled off from the SU-8 mould, and it was treated by oxygen plasma for 4 min at an RF power of 18 W to activate the surface to gain reactive silanol functional groups

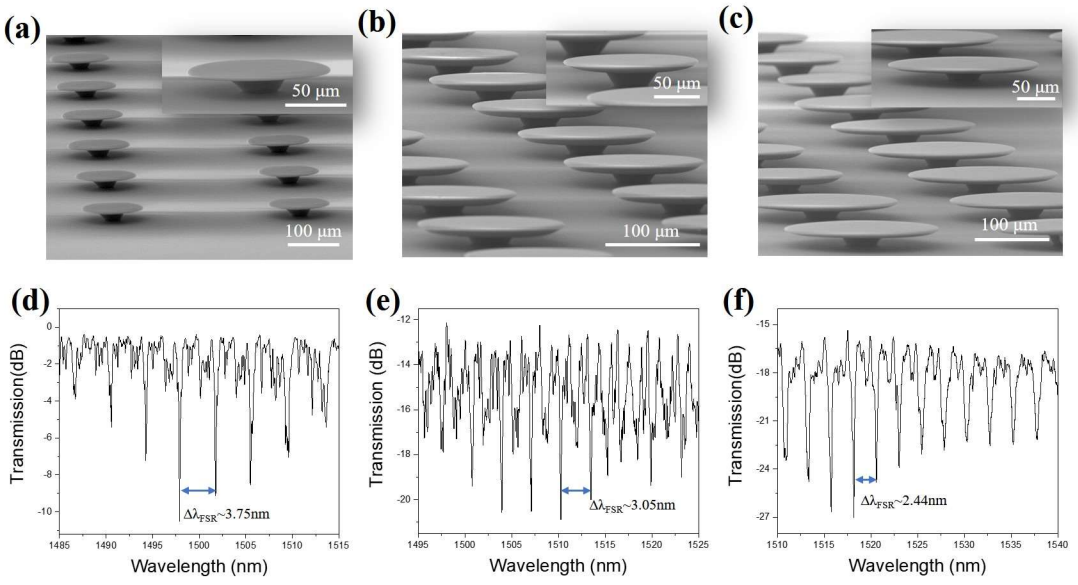

Fig. 2 (a)-(c) SEM images of optical 3D-printed polymer WGMC-1, WGMC-2 and WGMC-3, respectively. The insets are the corresponding magnified SEM images. (d)-(f) Transmission spectra of WGMC-1, WGMC-2 and WGMC-3, whose Q-factors are approximately 9800, 7000 and 5800, respectively.

(Fig. S3). The treated PDMS sheet was then combined with the silanized substrate after precise alignment. The microfluidic chip was then baked in the oven at 70 °C for 30 min to enhance the bonding between PDMS and the substrate.

Results

Directly printed WGM microcavity lasers

Polymer WGM microcavities of suspended microdisk structure were directly printed by using optical μ-printing technology (see the Methods). Compared with our previous results,[30] an improved printing process technology with a newly established relation between exposure dose and cured depth was developed to rapidly print WGM microcavities with relatively high *Q*-factors. Fig. 2a, 2b and 2c show the scanning electron microscopy (SEM) images of the three groups of fabricated SU-8 WGM microcavities, which were denoted as WGMC-1, WGMC-2, and WGMC-3. The diameters of the three groups of microcavities were 116, 146, and 195 μm. Notably, the exposure time of printing such large-scale arrayed intricate microcavities was as short as 46 s, which thus provides an approach to the rapid fabrication of high-quality WGM microcavities for the development of cost-effective photonic biochips.

The transmission spectra of WGMC-1, WGMC-2 and WGMC-3, which were measured with taped biconical optical fibres,[31] are shown in Fig. 2d-2f. Their measured average free-space ranges (FSRs) were 3.75, 3.05, and 2.44 nm, respectively, which agreed well with the values estimated by using the refractive index of SU-8, *n*, and the diameter of the microcavities, *D*, in the equation $\lambda^2/(\pi nD)$, i.e., 3.91, 3.17 and 2.40 nm, respectively. From the measured transmission spectra, the *Q*-factors of the microcavities were calculated with

$$Q \approx \frac{\lambda_c}{\Delta\lambda_{FWHM}}, \quad (1)$$

where $\Delta\lambda_{FWHM}$ is the full width at half maximum (FWHM) of the Lorentzian-shaped resonance peak and λ_c is the central wavelength of the resonant peak. After fitting the resonant peaks with Lorentzian functions, the *Q*-factors of WGMC-1, WGMC-2 and WGMC-3 were calculated to be approximately 9800, 7000, and 5800, respectively. It can be seen that the optical microcavity with a relatively large diameter had a relatively low *Q*-factor, which may result from increased transverse displacement with the size increase of suspended microdisks.[32]

WGM microcavity lasers were fabricated by depositing an optical gain material upon the fabricated optical microcavities. The fluorescent images of the three groups of arrayed WGM microlasers (WGMLs), denoted as WGML-1, WGML-2, and WGML-3, corresponding to WGMC-1, WGMC-2 and WGMC-3, are shown in the insets of Fig. 3a, 3b and 3c, respectively. The arrayed WGMLs show good uniformity in the same batch of fabricated microcavities. Resulting from the whispering-gallery modes, rings of orange fluorescent light appeared around the periphery of the WGMLs. The lasing thresholds of the three different WGMLs were characterized by measuring the output light intensity with increasing pulse energy of the pump laser, as shown in Fig. 3a-3c. The laser thresholds of WGML-1 to WGML-3 in terms of pump pulse energy were measured to be as low as 25.06, 131.38, and 141.61 nJ/mm^2, respectively.

To test the measured laser threshold, the Purcell enhancement factor *F* was calculated by using the *Q*-factor and the effective mode volume V_{eff} calculated with the finite element method (COMSOL Multiphysics 5.1) as [16, 33]

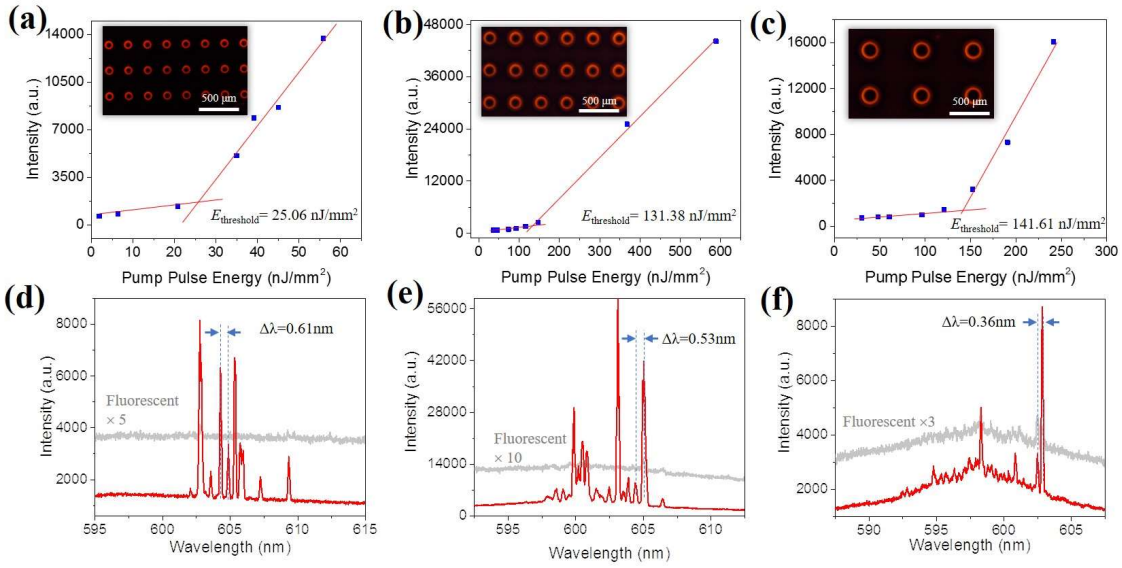

Fig. 3 Lasing characteristics of WGM microlasers. (a)-(c) Pump-output curves of WGML-1, WGML-2 and WGML-3, respectively. Insets are the fluorescent images of the corresponding WGML array. (d)-(f) Measured spectra of WGML-1, WGML-2 and WGML-3 when their pump pulse energies were 44.83, 588.51, and 190.8 nJ/mm^2, respectively. The grey curves are the fluorescent spectra of WGML-1, WGML-2 and WGML-3 when their pump pulse energies were 20.69, 116.09, and 120.69 nJ/mm^2, respectively.

$$F = \frac{3Q(\lambda_c/n)^3}{4\pi^2 V_{eff}} \approx 4.16\times10^{-21}\frac{Q}{V_{eff}}, \quad (2)$$

where λ_c represents the central wavelength of the lasing mode and n is the refractive index of the optical microcavity. The simulated electric field distribution and calculation of the effective mode volume of the fundamental mode of the WGMLs at approximately 604 nm are shown in Fig. S4. The calculated Purcell enhancement factors of WGML-1, WGML-2 and WGML-3 were 0.097, 0.048 and 0.023, respectively. The results indicated that WGML-1 had the lowest laser threshold due to the largest F, which agreed well with the experimental results.

Figures 3d-3f show the measured spectra of WGML-1, WGML-2 and WGML-3 under different pump pulse energies, i.e., 44.83, 588.51, and 190.8 nJ/mm^2, respectively. The measured spectral peak intervals of the laser emissions were 0.61, 0.53 and 0.36 nm, respectively, which agreed well with the calculated FSRs of WGMC-1, WGMC-2 and WGMC-3, i.e., 0.63, 0.51, and 0.38 nm, respectively. The matched measured and calculated FSRs indicated that the optical feedback provided by the optical microcavities assisted in laser oscillation. When the pulse energy of the pump laser was lower than the laser threshold, i.e., 20.69 nJ/mm^2 for WGML-1, 116.09 nJ/mm^2 for WGML-2, and 120.69 nJ/mm^2 for WGML-3, only weak fluorescence spectra were observed, as shown in Fig. 3d-3f. The intensity of the laser peaks was much higher than that of fluorescent light, which provided a signal with a high-contrast ratio for laser intensity-based biosensing applications.

WGML-integrated optofluidic biochip

The WGMLs were integrated into a microfluidic chip to fabricate an optofluidic chip for on-chip ELISA via chromogenic reaction, i.e., catalysing chromogenic substrates by enzymes.[34] A photo of the fabricated optofluidic chip is shown in Fig. 4a. The microfluidic chip was designed with multiple inlets and a spiral mixer for delivering and mixing reagents and biomolecules by means of microfluidics. As shown in the inset of Fig. 4a, the WGMLs located along the centre line of the main microchannel and fishbone-shaped side channels were fabricated to allow for the insertion of MMOFs for pumping and collecting laser emission from WGMLs. Such an optofluidic chip combined the merits of microfluidic chips and high-Q WGMLs and thus provided a promising platform for on-chip chromogenic reaction-based bioassays, such as ELISA.

Before ELISA experiments, the sensing performance of the WGML biosensor-integrated optofluidic chip was tested by measuring the detectable concentration of HRP-streptavidin via chromogenic reaction, in which HRP hydrolyses hydrogen peroxide (H_2O_2) to produce oxygen radicals that can oxidize 3,3',5,5'-tetramethylbenzidine (TMB) and then result in a colour change.[34] In the experiments, a 160-μL mixture of TMB colour reagent A (H_2O_2-containing solution) and B (TMB-containing solution) at a ratio of 1:1 was injected and mixed with an HRP-streptavidin solution in the microchannel of the on-chip spiral mixer. The mixed solution was then incubated in the microchannels around the WGMLs for 40 min.[8, 22] Thereafter, the light emitted from the WGMLs was collected by MMOFs and

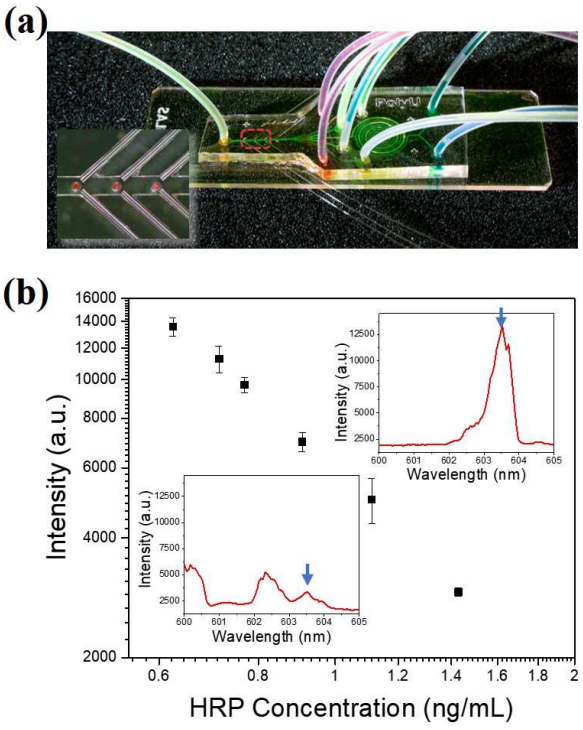

Fig. 4 (a) Photo of the fabricated optofluidic chip. The inset shows the on-chip integrated WGMLs coupled with MMOFs. (b) Laser intensity as a function of the concentration of HRP-streptavidin on a log-log scale. The top right and bottom left insets are the laser spectra corresponding to HRP-streptavidin concentrations of 0.625 and 1.43 ng/mL, respectively.

measured by a portable spectrometer for analysis of HRP-streptavidin concentration.

The concentration of the catalyst, i.e., HRP-streptavidin, in the microchannel determines the amount of catalytic reaction product. When the concentration of the product is very low, the relation of the concentration of catalyst E and the product of the catalytic reaction P can be derived from the Michaelis-Menten equation as[35]

$$P = C_0[1 - e^{(-\frac{k_c E}{K_m}t)}], \quad (3)$$

where k_c is the turnover number, t is the reaction time, C_0 denotes the initial substrate concentration, and K_m represents the Michaelis-Menten constant. At a certain reaction time t, with increasing catalyst concentration, the concentration of the reaction product will increase. The catalytic reaction product will absorb visible light, which thus leads to a loss in optical signal. The relation between the intensity of laser output I_{laser} and optical losses can be written as[36]

$$I_{Laser} \propto I_{pump} c_e \left(\frac{g}{c_e + c_a\delta_{in} + c_b\delta_{ex}} - 1\right), \quad (4)$$

where I_{pump} is the pump laser intensity, and c_e, g, δ_{in} and δ_{ex} denote the coefficients of external cavity coupling, optical gain, intrinsic and external optical losses, respectively. c_a and c_b are the coefficients related to optical mode distribution. The intrinsic optical loss δ_{in} is inversely proportional to Q-factor,[37]

and the external optical loss δ_{ex} here mainly depends on the concentration of coloured product *P* in a chromogenic reaction, which leads to a signal of light intensity of the WGML biosensor.

The absorbance spectra of TMB with and without catalysis by HRP are shown in Fig. S5, in which one can clearly see the absorption peak ranging from 600 nm to 700 nm. Notably, the acid stop solution was not used in the experiment because it shifted the absorption peak to approximately 450 nm and thus led to a mismatch between the absorbance spectrum of the catalysed TMB and the emission spectra of the WGMLs.

The measured variation of the laser output with respect to the concentration of the HRP-streptavidin solution from 0.625 to 1.43 ng/mL is depicted in Fig. 4b. The intensity of the laser output peak at a wavelength of approximately 603.5 nm, as shown in the inset of Fig. 4b, was tracked, where a pump laser pulse energy of 44.83 nJ/mm^2 was used in the experiment. The error bars represent the standard deviation of laser intensities measured from 10 measurements. The measured FWHW of the laser output was larger than that shown in Fig. 3d, which may have resulted from the relatively low resolution of the portable spectrometer. Nevertheless, its influence on the measurement resolution was small because of the use of the laser intensity-modulation-based signal interrogation method. On the log-log scale, the laser output intensity decreased linearly with increasing HRP-streptavidin concentration, as expected.

The limit of detection (LOD) of such a laser intensity-modulation-based biosensor is estimated by $3S_a/b$,[38] in which S_a is the standard deviation of the measured data and *b* represents the slope of the dependence curve of the laser output intensity with respect to the concentration of HRP-streptavidin. With the numerically fitted slope and the calculated deviation at the point with the lowest measured concentration, i.e., 0.625 ng/mL, the LOD for the detection of HRP-streptavidin was calculated to be 0.3 ng/mL.

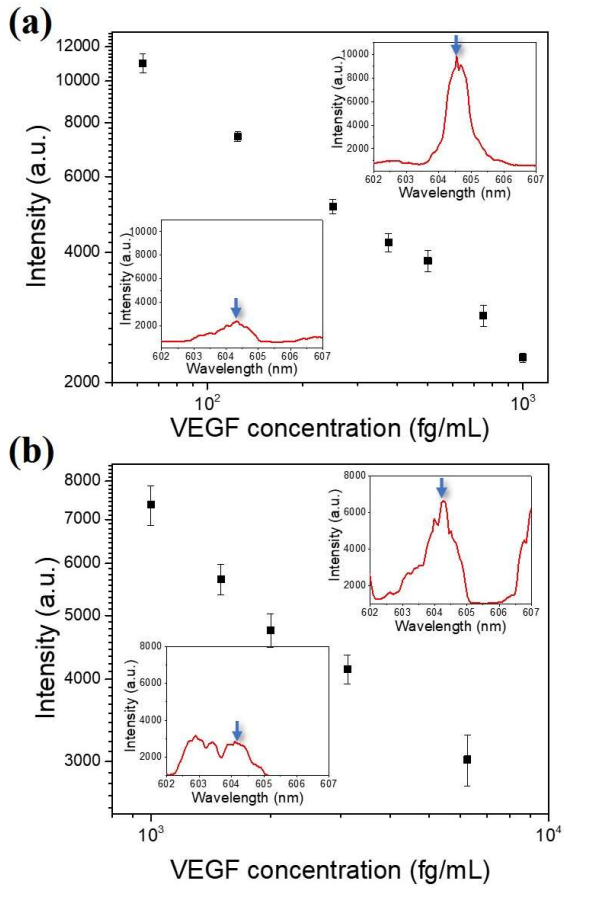

Fig. 5 Measured laser output intensity with respect to the concentration of VEGF. (a) The pump pulse energy was 44.83 nJ/mm^2. The top right and bottom left insets are the measured spectra when the VEGF concentration was 65 and 10^3 fg/mL, respectively. (b) The pulse energy of the pump laser was 112.64 nJ/mm^2. The top right and bottom left insets are the measured spectra when the VEGF concentration was 10^3 and 6.25×10^3 fg/mL, respectively.

On-chip optofluidic ELISA of VEGF

Because of both high specificity and high sensitivity, chromogenic reaction-based ELISA is widely used as a benchmarking analytical biochemistry assay in the detection of biomarkers. The WGML biosensor-integrated optofluidic chip was specially designed for on-chip microfluidic ELISA. Compared with the procedures used for the detection of HRP-streptavidin, the ELISA process required the functionalization of the surface of the WGMLs with a specific antibody for the target biomolecule, i.e., VEGF, before the execution of the chromogenic reaction. The adoption of on-chip, high-*Q* WGML biosensors could enhance the signal-noise ratio of the biosensing microsystem to achieve an ultrasensitive ELISA product.

In the experiments, 0.1 mL diluted capture antibody (1 μg/mL in PBS) of the target antigen was injected from inlet 1 (Fig. 1a) and then incubated in the microchannel around the WGMLs overnight at room temperature (RT) to immobilize the antibody on the silanized surface of WGMLs. Then, the on-chip WGMLs were flushed with wash buffer (0.05% Tween 20 in PBS), which was injected via inlet 7, and then blown with air via inlet 8. The above wash processes were repeated 3 times to fully remove the residual reagents from the WGMLs. Reagent diluent (1% BSA in PBS) was then injected via inlet 7 to incubate the microchannel at RT for 2 h to block any un-immobilized areas. After completing another 3 washes for removing the remaining reagent diluent, 0.2 mL target biomolecule, i.e., VEGF, in reagent diluent was injected into the microchannel via inlet 2 and statically incubated around the WGMLs at RT for 2 h. Thereafter, 0.5 mL diluted biotinylated detection antibody (100 ng/mL) in reagent diluent , which provides a stable environment and prevents unspecific binding with the antibody, was injected through inlet 3 and incubated for 2 h at RT to achieve a sandwich structure for high-specificity ELISA. After washing out the unbound detection antibody, 0.2 mL HRP-streptavidin (30 ng/mL) was injected into the microchannel with the WGMLs from inlet 4 and incubated at RT for 20 min to bind with the biotinylated detection antibody via binding between streptavidin and biotin. Thereafter, the microchannel was washed 3 times to completely remove residual material. Finally, TMB colour reagent A and B were injected via inlet 5 and inlet 6, respectively, and mixed through the on-chip spiral mixer and

then incubated in the microchannel around the WGMLs for 40 min to achieve chromogenic reaction. The assay time is around 5.5 hr.

Figure 5 shows the measured results under different pump pulse energies, in which the intensity of the laser peak at the central wavelength of approximately 604.5 nm (as shown in the top right inset of Fig. 5a) was recorded. Fig. 5a shows the measured result (in log-log scale) corresponding to the VEGF concentration ranging from 65 fg/mL to 10^3 fg/mL when the pump pulse energy was 44.83 nJ/mm^2. The laser output intensity decreased logarithmically with increasing VEGF concentration. When the VEGF concentration was 10^3 fg/mL, the tracked laser peak was weak (Fig. 5a bottom left inset) because of high optical loss. To extend the detection range for higher detection concentrations, the pump pulse energy was increased to 112.64 nJ/mm^2 in the experiment. Correspondingly, the laser output intensity was extended to 6.75×10^3 fg/mL, as shown in Fig. 5b. The FWHM of the laser peak, as shown in the top right inset of Fig. 5b, was broader than that at a lower pumping power, which may have resulted from more excited lasing WGMs.[39]

With the standard deviation of the measured data and the slope of the dependence curve, the LOD of the microfluidics-driven WGML biosensor under the pump pulse energy of 44.83 nJ/mm^2 was calculated to be 17.8 fg/mL. Notably, the LOD of the fabricated WGML biosensor was 2 orders of magnitude lower than that of commercial ELISA kits, whose LOD is typically on the pg/mL level.[5,40] Compared with other ultrasensitive sensors of VEGF, the WGML biosensor show comparable sensing performance with the sensors using surface-enhanced Raman spectroscopy, whose LOD is approximately 1 fg/mL,[29] meanwhile the WGML biosensor-based on-chip microfluidic ELISA microsystem exhibited the advantages of low cost and potential in portable applications.

Discussion and conclusion

Thanks to the high precision and high repeatability of the optical printing technology, the geometric uniformity of the same type of WGMCs is good and the variation of their Q-factors is not significant. It helps to minimize the influence of the variation of Q-factors on the translation of analyte concentration as the intensity of microlaser output is affected by the variation of Q-factors in a certain degree. The performance of such a WGML biosensor-integrated biochip may be further improved to achieve a lower LOD by improving the stability of the WGMLs and increasing the sensitivity of the WGML biosensors. The stability of the WGMLs can be improved if a more stable pump laser can be used and/or the fluctuation of pump laser output can be compensated.[41] The sensitivity of the WGML biosensor can be increased by optimizing the geometry of the WGM microcavity. In particular, the periphery of the WGM microcavity can be optimized to engineer the distribution of whispering-gallery modes[42], and thereby increase the light and molecular interactions around the periphery of the WGM microcavity. Moreover, specially designed WGMLs, such as dual-colour lasers, can be devised to enable the laser sensor with self-reference ability, e.g., two separate spectral components of the laser could be used for sensing and reference to minimize the deviation of the output signal.[43]

Notably, multiple WGMLs can be integrated within one optofluidic chip, as shown in the inset of Fig. 4a. With a specially designed microfluidic chip with multiple channels or inkjet printing technology,[44, 45] WGMLs can be functionalized by using different antibodies. Therefore, the optofluidic chip can be used to simultaneously detect multiple biomolecules, such as interleukin-6, tumour necrosis factor and interferon, from one liquid sample. Such a technology may be able to totally unlock the synergistic potential of microfluidics and microphotonics to achieve a "lab-on-a-chip" device to detect multiple biomarkers at extremely low levels for the diagnosis of early-stage diseases.

In summary, we have presented an optofluidic chip integrated with 3D μ-printed high-Q WGM microlasers for on-chip microfluidic ELISA. An improved optical 3D μ-printing technology has been established to rapidly fabricate multiple high-Q WGM microcavities. Low-threshold WGM microlasers have been demonstrated and integrated into a microfluidic chip for on-chip microfluidic ELISA. Experimental results revealed that the polymer WGML biosensor-integrated optofluidic chip can enable ELISA of VEGF at the level of 17.8 fg/mL. Such a polymer WGML biosensor-integrated optofluidic technology provides a pathway to synergistically integrate photonics and microfluidics to develop cost-effective high-performance biochips for ultrasensitive detection of multiple biomarkers for early-stage disease diagnosis.

Author contributions

Experiments were designed by X.O. and A.P.Z. X.O. carried out the fabrication and testing experiments. T.L. and Y. Zhang participated in the characterization and measurement of biosensors. J.H. participated in the characterization of microlasers. Z.H. participated in the fabrication of microcavities. H.-Y.T. participated in the experimental design and provided feedback on the experiments. Data analysis and interoperation were performed by X.O. and A.P.Z. The manuscript was written by X.O. and A.P.Z. with input from all authors.

Conflicts of interest

There are no conflicts of interest to declare.

Acknowledgements

We would like to thank Dr. Yunfeng Wang, Mr. Siqi Li and Ms. Yubing Hu for the testing setup and Dr. Chaoyang Gong for helpful discussion. We acknowledge financial support from the Hong Kong RGC General Research Fund (Grant No.: PolyU 152211/19E), PolyU Strategic Development Special Project (Grant No.: 1-ZVGB) and PolyU General Research Fund (Grant No.: G-YBY2).

References

1. M. S. Pepe, R. Etzioni, Z. Feng, J. D. Potter, M. L. Thompson, M. Thornquist, M. Winget and Y. Yasui, *JNCI: Journal of the National Cancer Institute*, 2001, **93**, 1054-1061.
2. D. M. Rissin, C. W. Kan, T. G. Campbell, S. C. Howes, D. R. Fournier, L. Song, T. Piech, P. P. Patel, L. Chang, A. J. Rivnak, E. P. Ferrell, J. D. Randall, G. K. Provuncher, D. R. Walt and D. C. Duffy, *Nat Biotechnol*, 2010, **28**, 595-599.
3. R. de la Rica and M. M. Stevens, *Nat Protoc*, 2013, **8**, 1759-1764.
4. D. A. Giljohann and C. A. Mirkin, *Nature*, 2009, **462**, 461-464.
5. S. Dehghani, R. Nosrati, M. Yousefi, A. Nezami, F. Soltani, S. M. Taghdisi, K. Abnous, M. Alibolandi and M. Ramezani, *Biosens Bioelectron*, 2018, **110**, 23-37.
6. M. Y. Hsu, Y. C. Hung, D. K. Hwang, S. C. Lin, K. H. Lin, C. Y. Wang, H. Y. Choi, Y. P. Wang and C. M. Cheng, *Sci Rep*, 2016, **6**, 34631.
7. R. de la Rica and M. M. Stevens, *Nat Nanotechnol*, 2012, **7**, 821-824.
8. X. Wu, M. K. Oo, K. Reddy, Q. Chen, Y. Sun and X. Fan, *Nat Commun*, 2014, **5**, 3779.
9. X. Tan, Q. Chen, H. Zhu, S. Zhu, Y. Gong, X. Wu, Y.-C. Chen, X. Li, M. W.-H. Li, W. Liu and X. Fan, *ACS Sensors*, 2020, **5**, 110-117.
10. Y.-F. Xiao and Q. Gong, *Science Bulletin*, 2016, **61**, 185-186.
11. I. Spotts, C. A. Leclerc and C. M. Collier, *Appl Opt*, 2019, **58**, 7904-7908.
12. A. Kiraz, Q. Chen and X. Fan, *ACS Photonics*, 2015, **2**, 707-713.
13. L. He, Ş. K. Özdemir and L. Yang, *Laser & Photonics Reviews*, 2013, **7**, 60-82.
14. T. Grossmann, S. Schleede, M. Hauser, M. B. Christiansen, C. Vannahme, C. Eschenbaum, S. Klinkhammer, T. Beck, J. Fuchs, G. U. Nienhaus, U. Lemmer, A. Kristensen, T. Mappes and H. Kalt, *Applied Physics Letters*, 2010, **97**, 063304.
15. S. Zhu, L. Shi, S. Yuan, R. Ma, X. Zhang and X. Fan, *Nanophotonics*, 2018, **7**, 1669-1677.
16. T. Reynolds, N. Riesen, A. Meldrum, X. Fan, J. M. M. Hall, T. M. Monro and A. François, *Laser & Photonics Reviews*, 2017, **11**, 1600265.
17. L. Jin, Y. Wu, Y. Wang, S. Liu, Y. Zhang, Z. Li, X. Chen, W. Zhang, S. Xiao and Q. Song, *Adv Mater*, 2018, 1807079.
18. L. Wan, H. Chandrahalim, J. Zhou, Z. Li, C. Chen, S. Cho, H. Zhang, T. Mei, H. Tian, Y. Oki, N. Nishimura, X. Fan and L. J. Guo, *Opt Express*, 2018, **26**, 5800-5809.
19. L. He, S. K. Ozdemir, J. Zhu, W. Kim and L. Yang, *Nat Nanotechnol*, 2011, **6**, 428-432.
20. U. Bog, F. Brinkmann, H. Kalt, C. Koos, T. Mappes, M. Hirtz, H. Fuchs and S. Kober, *Small*, 2014, **10**, 3863-3868.
21. S. F. Wondimu, S. von der Ecken, R. Ahrens, W. Freude, A. E. Guber and C. Koos, *Lab Chip*, 2017, **17**, 1740-1748.
22. C. Gong, Y. Gong, X. Zhao, Y. Luo, Q. Chen, X. Tan, Y. Wu, X. Fan, G. D. Peng and Y. J. Rao, *Lab Chip*, 2018, **18**, 2741-2748.
23. W. Lee, Q. Chen, X. Fan and D. K. Yoon, *Lab Chip*, 2016, **16**, 4770-4776.
24. T. Wienhold, S. Kraemmer, S. F. Wondimu, T. Siegle, U. Bog, U. Weinzierl, S. Schmidt, H. Becker, H. Kalt, T. Mappes, S. Koeber and C. Koos, *Lab Chip*, 2015, **15**, 3800-3806.
25. S. F. Wondimu, M. Hippler, C. Hussal, A. Hofmann, S. Krammer, J. Lahann, H. Kalt, W. Freude and C. Koos, *Opt Express*, 2018, **26**, 3161-3173.
26. Y. L. Sun, Z. S. Hou, S. M. Sun, B. Y. Zheng, J. F. Ku, W. F. Dong, Q. D. Chen and H. B. Sun, *Sci Rep*, 2015, **5**, 12852.
27. Z. Zhang, N. Yao, J. Pan, L. Zhang, W. Fang and L. Tong, *Nanoscale*, 2019, **11**, 5203-5208.
28. X. Ouyang, Z. Yin, J. Wu, C. Zhou and A. P. Zhang, *Optics Express*, 2019, **27**, 18376-18382.
29. D. Sun, F. Cao, W. Xu, Q. Chen, W. Shi and S. Xu, *Anal Chem*, 2019, **91**, 2551-2558.
30. J. Wu, X. Guo, A. P. Zhang and H. Y. Tam, *Opt Express*, 2015, **23**, 29708-29714.
31. G. Zhao, Ş. K. Özdemir, T. Wang, L. Xu, E. King, G.-L. Long and L. Yang, *Science Bulletin*, 2017, **62**, 875-878.
32. M. L. Dunn, Y. Zhang and V. M. Bright, *Journal of Microelectromechanical Systems*, 2002, **11**, 372-384.
33. E. M. Purcell, in *Confined Electrons and Photons: New Physics and Applications*, eds. E. Burstein and C. Weisbuch, Springer US, Boston, MA, 1995, pp. 839-839.
34. E. S. Bos, A. A. van der Doelen, N. van Rooy and A. H. Schuurs, *J Immunoassay*, 1981, **2**, 187-204.
35. J. G. Wagner, *Journal of Pharmacokinetics and Biopharmaceutics*, 1973, **1**, 103-121.
36. A. E. Siegman, *Lasers, University Science Books*, 1986.
37. M. L. Gorodetsky, A. A. Savchenkov and V. S. Ilchenko, *Optics Letters*, 1996, **21**, 453-455.
38. A. Shrivastava and V. Gupta, *Chronicles of Young Scientists*, 2011, **2**.
39. R. S. Quimby, *Photonics and lasers : an introduction*, John Wiley, Hoboken, NJ, 2006.
40. H. Takahashi, Y. Nomura, J. Nishida, Y. Fujino, Y. Yanagi and H. Kawashima, *Invest Ophthalmol Vis Sci*, 2016, **57**, 462-466.
41. M. Bukshtab, *Photometry, Radiometry, and Measurements of Optical Losses*, Singapore, 2019.
42. S. M. Spillane, T. J. Kippenberg, K. J. Vahala, K. W. Goh, E. Wilcut and H. J. Kimble, *Physical Review A*, 2005, **71**.
43. A. Vallan, M. L. Casalicchio, M. Olivero and G. Perrone, *IEEE Transactions on Instrumentation and Measurement*, 2012, **61**, 1377-1383.
44. U. Bog, T. Laue, T. Grossmann, T. Beck, T. Wienhold, B. Richter, M. Hirtz, H. Fuchs, H. Kalt and T. Mappes, *Lab Chip*, 2013, **13**, 2701-2707.
45. C. F. Carlborg, K. B. Gylfason, A. Kazmierczak, F. Dortu, M. J. Banuls Polo, A. Maquieira Catala, G. M. Kresbach, H. Sohlstrom, T. Moh, L. Vivien, J. Popplewell, G. Ronan, C. A. Barrios, G. Stemme and W. van der Wijngaart, *Lab Chip*, 2010, **10**, 281-290.

Supplementary information for

Ultrasensitive optofluidic enzyme-linked immunosorbent assay by on-chip integrated polymer whispering-gallery-mode microlaser sensors

Xia Ouyang,[a] Tong Liu,[a] Yangxi Zhang,[a] Jijun He,[a,b] Zijian He,[a] A. Ping Zhang*[a] and Hwa-Yaw Tam[a]

The PDF file includes the following:

Fig. S1 (a) Schematic of optical 3D μ-printing technology. (b) Characterization of the relation between cure depth and exposure time: (i) Optical microscope image. (ii) 3D laser-scanning confocal image of fabricated SU-8 micropillars. (iii) Cured depth versus the exposure time on a natural-logarithm scale. Inset shows the dependence of cure depth on exposure time.

Fig. S2 Fabricated SU-8 mould for preparation of the microfluidic chip by the casting method. (a) Photo of SU-8 mould on silicon wafer. (b) Enlarged images of different parts. Scale bars are 500 μm.

Fig. S3 Treatments on the SU-8 surface for binding with PDMS or the antibody. (a) O_2 plasma treatment. (b) Silanization of the SU-8 surface by using aqueous APTES. (c) Binding with PDMS. (d) Binding with the antibody via electrostatic attraction.

Fig. S4 Simulation of the electric field distributions of the fundamental mode of WGMC-1 (a), WGMC-2 (b) and WGMC-3 (c). The radial mode numbers of the three abovementioned WGMs were calculated to be 940, 1186, and 1585, respectively. Scale bars are 2 μm.

Fig. S5 Comparison of the absorbance spectra of TMB and its mixture with HRP-streptavidin. The absorption peaks resulted from the catalytic product of TMB during chromogenic reaction.

[a] Photonics Research Center, Department of Electrical Engineering, The Hong Kong Polytechnic University, Hong Kong SAR, China. [b] Institute of Physics, École Polytechnique Fédérale de Lausanne (EPFL), CH-1015 Lausanne, Switzerland. *Correspondence and requests for materials should be addressed to A.P.Z. (email: azhang@polyu.edu.hk).

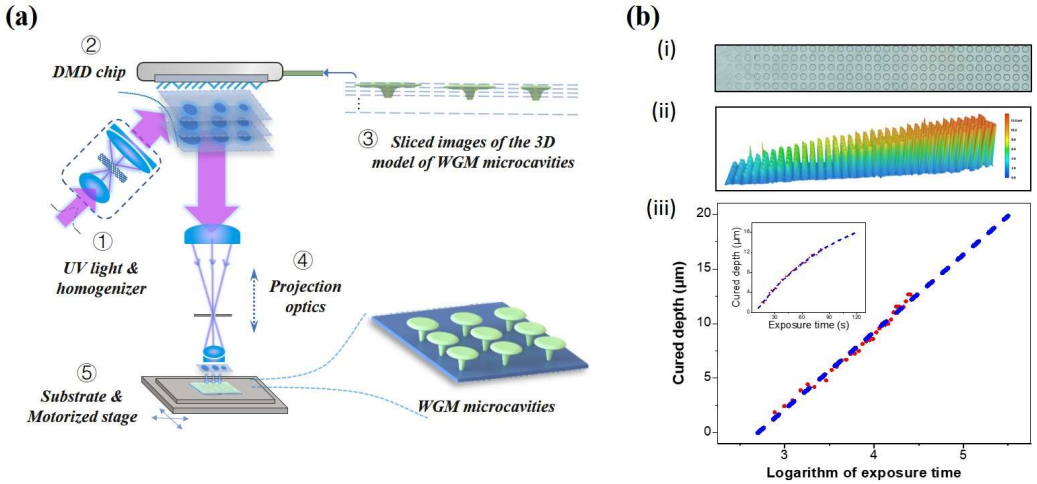

Fig. S1 (a) Schematic of optical 3D μ-printing technology. (b) Characterization of the relation between cure depth and exposure time: (i) Optical microscope image. (ii) 3D laser-scanning confocal image of fabricated SU-8 micropillars. (iii) Cured depth versus the exposure time on a natural-logarithm scale. Inset shows the dependence of cure depth on exposure time.

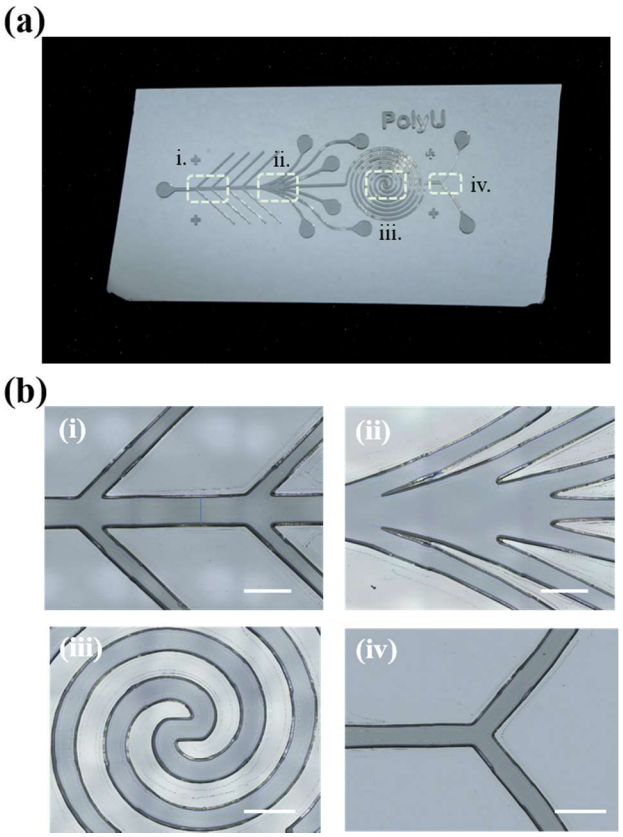

Fig. S2 Fabricated SU-8 mould for preparation of the microfluidic chip by the casting method. (a) Photo of SU-8 mould on silicon wafer. (b) Enlarged images of different parts. Scale bars are 500 μm.

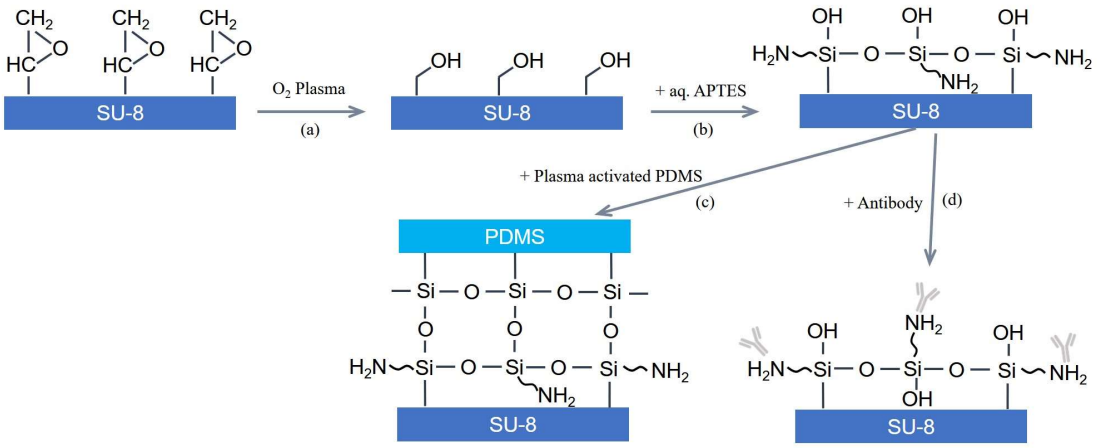

Fig. S3 Treatments on the SU-8 surface for binding with PDMS or the antibody. (a) O_2 plasma treatment. (b) Silanization of the SU-8 surface by using aqueous APTES. (c) Binding with PDMS. (d) Binding with the antibody via electrostatic attraction.

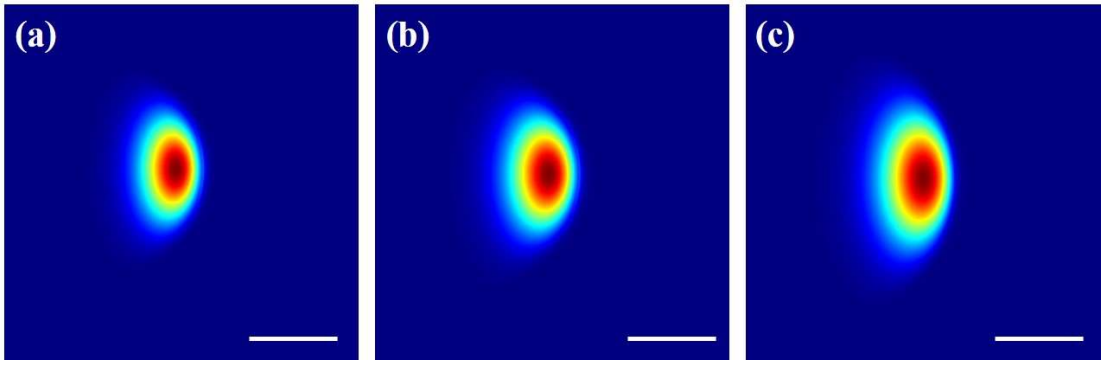

Fig. S4 Simulation of the electric field distributions of the fundamental mode of WGMC-1 (a), WGMC-2 (b) and WGMC-3 (c). The radial mode numbers of the three abovementioned WGMs were calculated to be 940, 1186, and 1585, respectively. Scale bars are 2 μm.

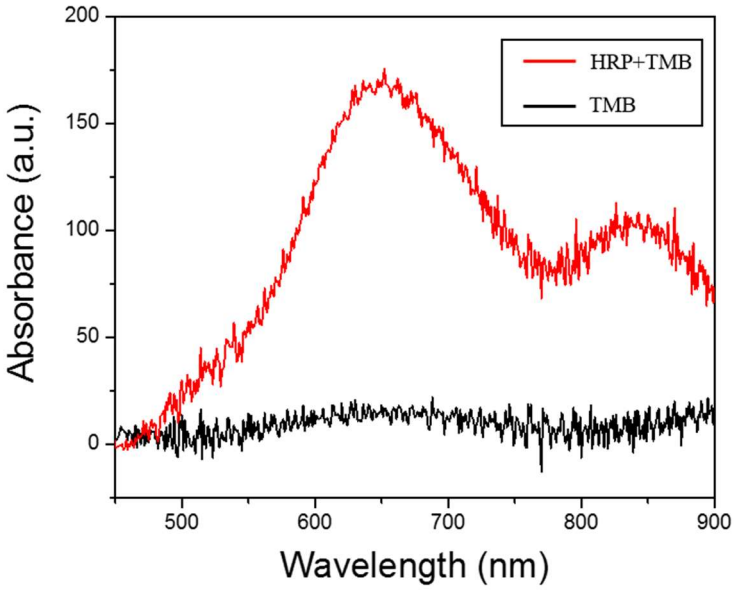

Fig. S5 Comparison of the absorbance spectra of TMB and its mixture with HRP-streptavidin. The absorption peaks resulted from the catalytic product of TMB during chromogenic reaction.